DEVELOPMENT AND TRIBOLOGICAL CHARACTERIZATION OF SEMI-METALLIC BRAKE PADS FOR AUTOMOTIVE APPLICATIONS

**P L ESTEEM[1], VAIRA VIGNESH RAMALINGAM[2],
RAJESH KANNAN KASI[3], PADMANABAN RAMASAMY[4]**

Abstract

Semi-metallic brake pads are quite a good choice for performance-driven automotive industries, because of improved braking performance in a more comprehensive range of temperatures. In this study, a semi-metallic brake pad is fabricated through a powder metallurgy processing technique with two compositions of powders with a different weight ratio of Copper (Cu), Iron (Fe), flash, Aluminum oxide (Al_2O_3), Barium sulfate ($BaSO_4$), Phenolic resin, Low-Density Polyethylene (LDPE), Graphite for automotive application. A well-distributed composition was indicated by the microstructure, which exhibited a uniform dispersion of hard particles throughout the matrix. BP-20Cu-20Fe specimen exhibited a high hardness value of 171Hv. Under higher loads of 70 N, the specimen BP-20Cu-20Fe showed excellent wear resistance, with a low wear rate of $1.072×10^{-6}$ g/Nm. On the other hand, specimen BP-20Cu-20Fe showed a notable 35% increase in friction coefficient when the load was increased from 30 N to 70 N. The surface morphology, elemental distribution, and worn surface features and characteristics are examined using advanced instrumental techniques.

Keywords: brake pads; automotive; tribology; wear; friction

1   Department of Mechanical Engineering, Amrita School of Engineering, Coimbatore, Amrita Vishwa Vidyapeetham, India, e-mail: esteempl40@gmail.com.

2   Department of Mechanical Engineering, Amrita School of Engineering, Coimbatore, Amrita Vishwa Vidyapeetham, India, e-mail: r.vairavignesh@gmail.com, ORCID: 0000-0002-6869-1763.

3   Department of Mechanical Engineering, Amrita School of Engineering, Coimbatore, Amrita Vishwa Vidyapeetham, India, e-mail: k_rajeshkannan@cb.students.amrita.edu.

4   Department of Mechanical Engineering, Amrita School of Engineering, Coimbatore, Amrita Vishwa Vidyapeetham, India, e-mail: dr_padmanaban@cb.amrita.edu.

1. Introduction

Brake pads are an indispensable component of an automobile braking system. The brake pad, which is housed inside the caliper, is the part of the brake system that presses down on the rotor. The brake pads eventually wear down due to the friction imparted to the disc to stop the wheel over time. In contrast to metallic brake pads, semi-metallic brake pads are added with a higher fraction of filler materials. Brake pads comprise 30% to 70% fraction of metals, including copper, iron, steel, and other alloys. The remaining fraction of the semi-metallic brake pads include binders, reinforcements, fillers, and friction reducers. Hence, semi-metallic brake pads are heterogeneous materials that are formulated with a range of physical, mechanical, and tribological properties.

The essential tribological features of semi-metallic brake pads are stable friction coefficient (brake pad against brake disc), adequate wear resistance (brake pad against brake disc), and superior fade resistance. The brake pads wear because of the friction against the brake disc. The wear rates and friction levels are influenced by the porosity, microstructure, and hardness of the friction layer that covers the surface of the brake pad or brake disc. The brake pads form wear debris in the form of particles or flakes. The wear debris produced in the course of the braking process also influences the wear rate and friction coefficient.

Semi-metallic brake pads are made of synthetic materials blended with different amounts of metal flakes and bounded with organic resin. They have more durability, fade resistance, and hardness than non-metallic pads, at the expense of faster rotor or drum replacement. To produce braking torque, they also need a higher actuating force than non-metallic pads. Semi-metallic brake pads are more heat resistant and gentler on rotors than their ceramic counterparts. They often cost less and with 60% or more metal fraction (Copper and Iron), are well suited for strong braking over a lengthy distance of track or road. Copper and Iron contribution to the brake pad is that it can resist high temperatures and also has the capability to provide smooth sliding conditions and good thermal handling capacity.

Yelong Xiao et al. [27] observed that Cu-based semi-metallic brake pads exhibited an elevated friction coefficient of 0.401 at 600°C, accompanied by a wear rate of 0.20 cm³/Nm. The research of Guha Keshav et al. [12] explicated that Cu-based brake pads demonstrated improved tribological characteristics, an optimized friction coefficient ranging between 0.3 and 0.4, and a minimal wear rate of 6.2×10^{-7} g/Nm. Yuji Handa et al. [6] noted that the inclusion of Cu powder led to a lower friction coefficient of 0.38 and a specific wear rate of 10^{-2}–10^{-4} (mm³/Nm). Mukesh Kumar et al. [14] examined the use of Cu as the best metallic filler, resulting in a reduced wear volume of 1.98×10^{-2} cc and friction coefficient ranging from 0.37 to 0.38. Gultekin et al. [5] found that Fe-based brake lining materials exhibited low wear rates (0.20 cm³/Nm) with a friction coefficient ranging between 0.2 and 0.45.

Phenolic resin, primarily used as a binder, provides thermal stability and resistance to high temperatures, along with properties like low smoke and good friction properties. M.A. Sai Balaji et al. [3] determined that the use of phenolic resins in semi-metallic disc brake pads resulted in 5.9% weighted wear loss, while alkyl benzene-modified resin showed 4.7% wear loss, with friction coefficient ranging between 0.35 and 0.45. Jianying Yu et al. [29] found that the presence of phenolic resin in brake pads resulted in a minimized wear rate and a friction coefficient of 0.39. S.K. Rhee et al. [24] suggested that the usage of phenolic resins in semi-metallic friction materials led to a lower wear rate of 0.21 to 0.32 (cm^3/Nm) with a friction coefficient of 0.45.

Solid lubricants, such as graphite, graphene, graphene oxides, hBN, and MoS2, are commonly used in particle form to reduce friction and wear on contacting surfaces. Hamid Reza Akram-ifard et al. [1] found that including graphite in a semi-metallic brake pad resulted in friction coefficient values ranging from 0.35 to 0.45 and a wear loss of 1.67%. The incorporation of hard particles in brake pads helps stabilize the friction coefficient at high braking speeds, imparting strength and hardness to withstand heavy loads during braking.

Vlastimil Matejka et al. [16] reported that the addition of 3% SiC improved tribological prop-erties with a friction coefficient of 0.34 and an optimized wear loss ranging between 10% and 15%. Pinca-Bretotean et al. [22] suggested that including 11% SiC resulted in an optimized friction coefficient of 0.35 and minimized wear of 0.06 g/Nm. The results were inline with the conclusions of Parikh et al. [21]. Samrat Mohanty et al. [18] concluded that the inclu-sion of fly ash in brake linings improved tribological characteristics, resulting in a minimum wear loss of 12% to 14% and friction coefficient ranging from 0.2 to 0.3. Venkata Naga Baji et al. [26] reported that using fly ash in semi-metallic brake pads yielded friction coefficient values between 0.35 and 0.45, along with a low wear rate of 0.29× cm^3/Nm. Satapathy et al. [10] studied the inclusion of vermiculite in fly ash-based fiber-reinforced hybrid composites, resulting in a wear behavior of $7.84×10^{-8}$ g/Nm and a low friction coefficient of 0.31.

Based on an extensive review of existing literature, it becomes evident that composite mate-rials dominate the investigations into friction materials for automobile applications. However, a notable gap persists in the development of diverse materials (polymers, ceramics, and metals) catering to high-performance friction needs. In light of this, the primary focus of this project is to enhance wear resistance and optimize the friction coefficient. A novel formula-tion for a semi-metallic brake pad has been developed, aimed specifically at improving wear resistance in the contact region between the brake pad and brake disc while simultaneously optimizing the friction coefficient.

2. Materials and Methodology

Materials

The brake pad formulation comprises various components, including Cu, Fe, phenolic resin, low-density polyethylene, graphite, flyash, aluminum oxide, and barium sulfate. In this study, Cu powder was utilized, having an average particle size of 75 µm and a purity of 99.9%. Fe powder was used with an average particle size of 75 µm and a purity of 99.5%. Graphite particles, averaging 150 µm in size with a purity of 97%, were employed. The fly ash originated from Mettur Thermal Power Plant, India, and had an average particle size of 15 µm. Al_2O_3 nanopowder used had an average particle size of 25 nm and a purity of 99.9%. Barium sulfate, with an average particle size of 50 µm and a purity of 98.2%, was included. Low-density polyethylene (LDPE) with an average particle size of 25 µm was utilized to improve bonding properties. Lastly, phenolic resin with a purity of 99% was incorporated as the binder.

Powder Metallurgy Processing

The obtained powders were carefully measured using a precision balance with a readability of 0.001g for each specimen, and the respective weights are presented in Table 1. Subsequently, the powders underwent a ball milling technique, and a small amount of binders were introduced. The powders were thoroughly mixed for one hour at a speed of 250 rpm.

Table 1. Composition of semi-metallic brake pads with specimen code

Sl.	Components	Composition (Weight [%])		
		BP-20Cu-20Fe	BP-10Cu-30Fe	BP-0Cu-40Fe
1	Copper	20	10	0
2	Iron	20	30	40
3	Phenolic Resin	20	20	20
4	LDPE	10	10	10
5	Graphite	10	10	10
6	Fly ash	10	10	10
7	Aluminum Oxide (Al_2O_3)	5	5	5
8	Barium Sulphate ($BaSO_4$)	5	5	5

The resulting mixture was then hydraulically compacted under a pressure of 250 MPa at room temperature. Afterward, the compacted specimen was placed inside a high-temperature furnace and cured at 195°C for a duration of 45 minutes, as illustrated in Figure 1.
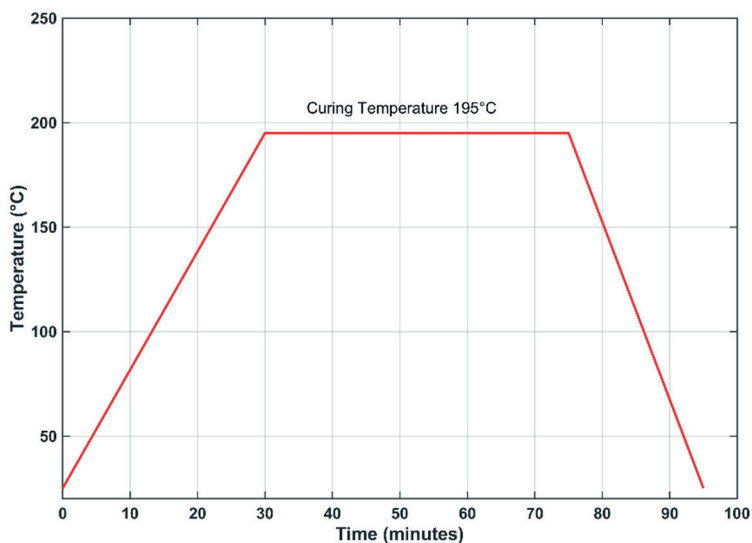
Fig. 1. Curing Cycle for the specimen

Microhardness

The specimens were prepared for microhardness testing, as per the ASTM E3–11 guidelines. The Vicker's microhardness of the specimens was determined using a microhardness tester (Make: Mitutoyo; Model: HVT – M1). For the hardness testing, an axial load of 100 g was applied for 15 s. Measurements were taken at five different locations on each specimen, and the average value was reported. Also, the hardness was measured using Brinell's hardness tester at an axial load of 10 N. The hardness was measured for five specimens and the average was reported.

Microstructure

The specimens were precisely prepared following the guidelines outlined in ASTM E3–11 for microstructure analyses. To ensure accurate observation, the specimens underwent a polishing process utilizing metallographic plates with different grit levels, including 400, 600, 800, 1000, and 1500. Once the polishing was completed, the specimens were subjected to microstructure examination using an optical microscope (Make: Carl Zeiss; Model: Axiovert 25).

Tribological characterization

The tribological properties of the specimens were evaluated using a pin–on–disc tribometer (Make: Ducom; Model: TR–20LE–PHM–200), as per the guidelines set by ASTM G99–5a. For the testing, three specimens were used, each measuring 20 mm in diameter. The specimens were placed within a hollow stainless–steel tube using a cold setting solution. Before the tribological tests, the specimens were cleaned with ethanol using an ultrasonicator. On the tribometer, the specimens were mounted and brought into contact with an EN–31 steel counter disc. To perform the tests, a lever arrangement setup was employed, applying axial loads of 30 N, 50 N, and 70 N on the specimens. The mass loss of each specimen was measured both before and after the tribological tests, with an accurate scale reading of 0.0001 g, to assess the wear characteristics and frictional behavior [8, 17].

Characterization using Analytical Instruments

The microstructure and worn surface of the specimens were investigated using a Field Emission Scanning Electron Microscope (SEM; Make: Zeiss Sigma; Model: Gemini 300) at electron acceleration voltages of 5 kV and 10 kV. The chemical compositions and elemental mapping of specimens were obtained using an energy–dispersive X–ray Spectroscope (EDS; Make: Oxford Instruments; Model: Ultima Max) at an electron–high tension of 20 kV. To analyze the constitutional phases, an X–ray Diffractometer (Make: Rigaku Model: Ultima 4) was utilized with Cu–Kα radiation as the X–ray source. The diffractometer operated in continuous scanning mode, scanning at a rate of 1° per minute over a range of 10° to 90°.
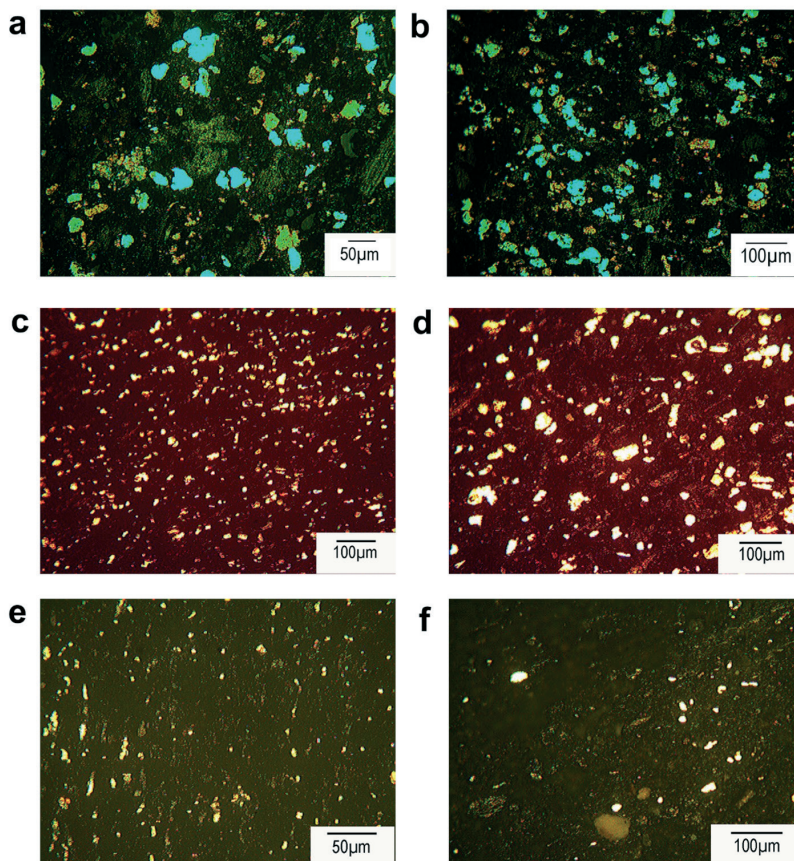
3. Results and Discussion

Microstructure

Fig. 2. Microstructure of specimen (a, b) BP 20Cu–20Fe; (c, d) BP 10Cu–30Fe, (e, f) BP 0Cu–40Fe

The illustrative representation of the microstructure characteristics of the cured specimens BP–20Cu–20Fe, BP–10Cu–30Fe, and BP–0Cu–40Fe are shown in Figure 2. The microstructural analysis revealed a uniform dispersion of various components, including Fe, Cu, Al_2O_3, $BaSO_4$, fly ash, graphite, and LDPE, across the samples. The regions colored in blue and reddish-brown distinctly denote the presence of iron and copper within the specimens respectively. The microstructures confirmed the variations in the concentration profile of copper and iron throughout the samples. A uniform distribution of both solid lubricant and reinforcing particles was observed, contributing to the overall structural integrity of the materials. The dark-gray regions are indicative of the presence of graphite. Additionally, visible pores were discerned in the cured specimens (BP–10Cu–30Fe and BP–0Cu–40Fe), primarily in proximity to the particles.

In Figure 2 (a) and Figure 2 (b) revealed a homogeneous dispersion of Fe, Cu, Al_2O_3, $BaSO_4$, fly ash, graphite, and LDPE throughout the specimen BP–20Cu–20Fe. The blue and reddish–brown regions within this microstructure distinctly represent the presence of equal fraction of copper and iron. Moreover, pores were note observed in the specimen BP–20Cu–20Fe. In the specimen BP–10Cu–30Fe shown in Figure 2 (c) and Figure 2 (d), the dispersion of Fe, Cu, Al_2O_3, $BaSO_4$, fly ash, graphite, and LDPE remains uniform and consistent. However, the specimen BP–10Cu–30Fe displayed visible pores, located near the particles. Furthermore, the distribution of solid lubricant and reinforcing particles was consistently uniform. The relative segregation of solid particles resulted in localized areas of higher density, leading to pore formation in adjacent regions [23, 25].

Figure 2 (e) and Figure 2 (f) shows the typical microstructure of the specimen BP–0Cu–40Fe. The microstructural analysis was consistent with the specimen BP–20Cu–20Fe and BP–10Cu–30Fe. The specimen had uniformity in the dispersion of various elements, including Fe, Cu, Al_2O_3, $BaSO_4$, fly ash, graphite, and LDPE. Similar to the specimen BP–10Cu–30Fe, visible pores were clustered near the particles. During the curing process, temperature gradients developed within the specimen. Localized heating and subsequent cooling affected the flow properties and potentially caused pores near particles. Also, localized rapid heating induced the release volatiles, creating voids [2, 13].
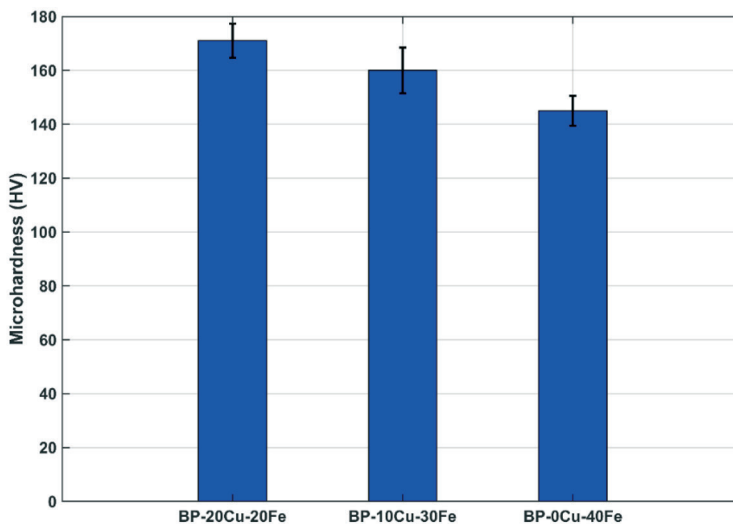
Microhardness

Fig. 3. Microhardness of the specimens

The average microhardness of the specimens BP–20Cu–20Fe, BP–10Cu–30Fe, and BP–0Cu–40Fe is shown in Figure 3. Among the tested specimens, the specimen BP–20Cu–20Fe exhibited the highest hardness, measuring ~171 HV (85 HRB). In contrast, the specimen BP–10Cu–30Fe displayed an intermediate hardness value of ~160 HV (81 HRB). The specimen BP–0Cu–40Fe demonstrated the lowest hardness value among the tested samples, measuring about ~145 HV (76 HRB). The specimen BP–20Cu–20Fe showcased a significant hardness advantage over BP–10Cu–30Fe and BP–0Cu–40Fe, being approximately 6.88% and 17.93% higher, respectively. Meanwhile, BP–10Cu–30Fe exhibited about 6.43% higher hardness than BP–0Cu–40Fe. The observations from the hardness profile indicate that as the fraction of Fe increases in the brake pad composition, the hardness of the specimen tends to decrease. This trend is evident, where the specimen BP–20Cu–20Fe with a balanced copper and iron content exhibited the highest hardness value, while the specimen BP–0Cu–40Fe with the highest fraction of Fe shows the lowest hardness value. The decrease in hardness with an increase in Fe fraction suggests that iron may have a softening effect on the brake pad material [7].
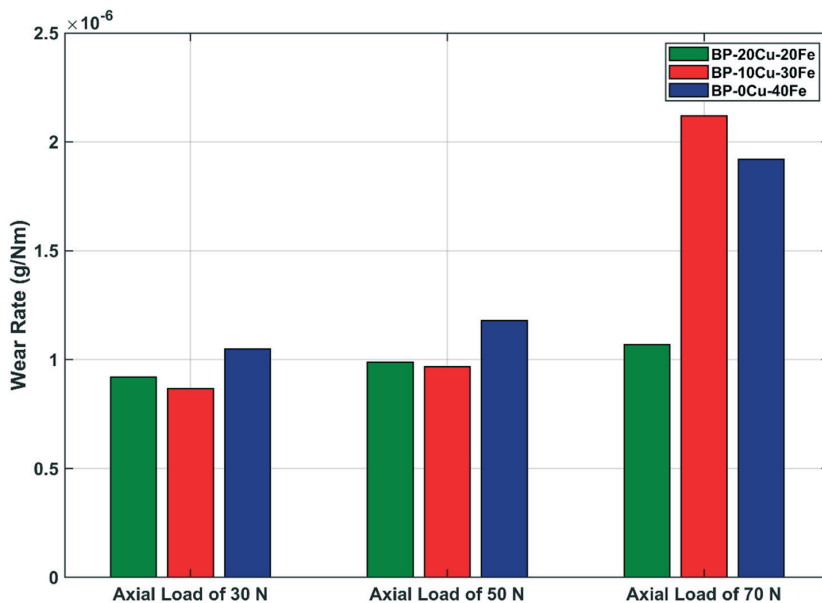
Tribological Characterization

Wear rate

Fig. 4. Wear rate of the specimens at normal load of 30 N, 50 N, and 70 N

Figure 4 shows the wear rate of the specimens was assessed using a pin–on–disc tribometer rig, subjecting them to various normal loads: 30 N, 50 N, and 70 N. At a normal load of 30 N, the specimen BP–20Cu–20Fe displayed a considerably low wear rate of 9.19×10^{-7} g/Nm. As the applied loads increased, the wear rate of BP–20Cu–20Fe exhibited a slight upward trend, reaching 1.07×10^{-6} g/Nm at 70 N. Similarly, at a normal load of 30 N, the wear rate of the specimen BP–10Cu–30Fe remained low, measuring within the range of 8.69×10^{-7} g/Nm. As the load was increased to 70 N, the wear rate of BP–10Cu–30Fe showed a slight decrease, reaching 2.12×10^{-6} g/Nm. Comparatively, at the load of 30 N, BP–20Cu–20Fe demonstrated a slightly higher wear rate than BP–10Cu–30Fe. However, with the increase in load to 70 N, the wear rate of BP–10Cu–30Fe surpassed that of BP–20Cu–20Fe.

The wear rate of the specimen BP–0Cu–40Fe was considerably low at 30 N, measuring at 1.05×10^{-6} g/Nm. However, as the load increased to 70 N, the wear rate of BP–0Cu–40Fe slightly increased to 1.920×10^{-6} g/Nm. Comparing the wear rates of BP–10Cu–30Fe and BP–0Cu–40Fe, at the load of 30 N, BP–10Cu–30Fe displayed a lower wear rate than BP–0Cu–40Fe. However, as the loads increased to 70 N, the wear rate of BP–10Cu–30Fe decreased slightly, while the wear rate of BP–0Cu–40Fe increased slightly.
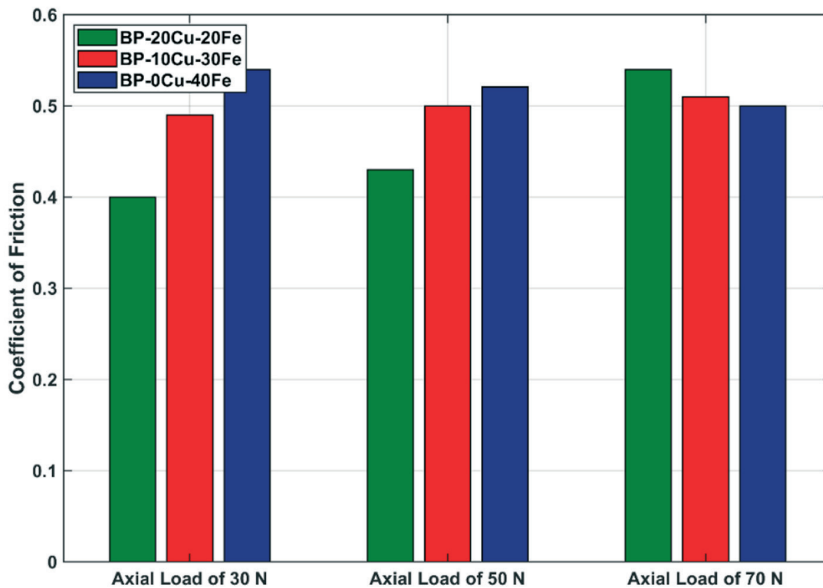
Friction Coefficient

Fig. 5. Friction coefficient of the specimens at normal load of 30 N, 50 N, and 70 N

Figure 5 depicts the relationship between the friction coefficient and applied loads for the specimens BP–20Cu–20Fe, BP–10Cu–30Fe, and BP–0Cu–40Fe. The graph illustrates that as the load increased, the friction coefficient also increased for the specimen BP–20Cu–20Fe. At a low load of 30 N, the friction coefficient was 0.40, suggesting reduced friction between the specimen and the counter disc. Conversely, at a load of 70 N, the friction coefficient reached a higher value of 0.54, indicating an increase in friction between the contact surfaces. The friction coefficient of the specimen The friction coefficient for the specimen BP–20Cu–20Fe exhibited a significant increase of about 35% as the load was increased from 30 N to 70 N.

BP–10Cu–30Fe demonstrated that the friction coefficient marginally increased with the load. At 70 N, the friction coefficient reaches a value of 0.51, while at lower loads of 30 N, it is 0.49. The specimen BP–10Cu–30Fe specimen showed a marginal increase of approximately 4% in friction coefficient as the load was increased from 30 N to 70 N. For the specimen BP–20Cu–20Fe, the friction coefficient showed a more significant increase from 0.40 to 0.54 (a difference of 0.14) when the load increased from 30 N to 70 N. However, for the specimen BP–10Cu–30Fe, the friction coefficient increased by a smaller margin from 0.49 to 0.51 (a difference of 0.02) over the same load range.

The friction coefficient of the BP–0Cu–40Fe specimen decreased as the load increased. At lower loads of 30 N, the friction coefficient was 0.54, suggesting an increase in friction between the contact surfaces of the specimen and the disc plate. Conversely, at a higher load of 70 N, the friction coefficient was measured to be 0.50, indicating a reduction in friction between the specimen and the counter disc. For the specimen, BP–10Cu–30Fe, the friction coefficient showed a meager increase from 0.49 to 0.51 (a difference of 0.02) when the load increased from 30 N to 70 N. However, for the specimen BP–0Cu–40Fe, the friction coefficient decreased by a smaller margin from 0.54 to 0.50 (a difference of 0.04) over the same load range [4].

Wear Mechanism at an Axial Load of 30 N
The surface characteristics of the cured specimen BP–20Cu–20Fe, subjected to a normal load of 30 N, are illustrated in Figure 6. Multiple surface irregularities, including debris, grooves, scratches, scoring marks, and pits were observed on the worn surface, as shown Figure 6 (a) and Figure 6 (b). The formation of grooves was attributed to the localized furrowing effect induced by the application of localized load. Scratches were the consequence of friction between the surface, as reported in previous studies. Furthermore, due to the rotational motion of the counter disc, the removal material resulted in the formation of chips, as depicted in Figure 6 (c) and Figure 6 (d) [19].
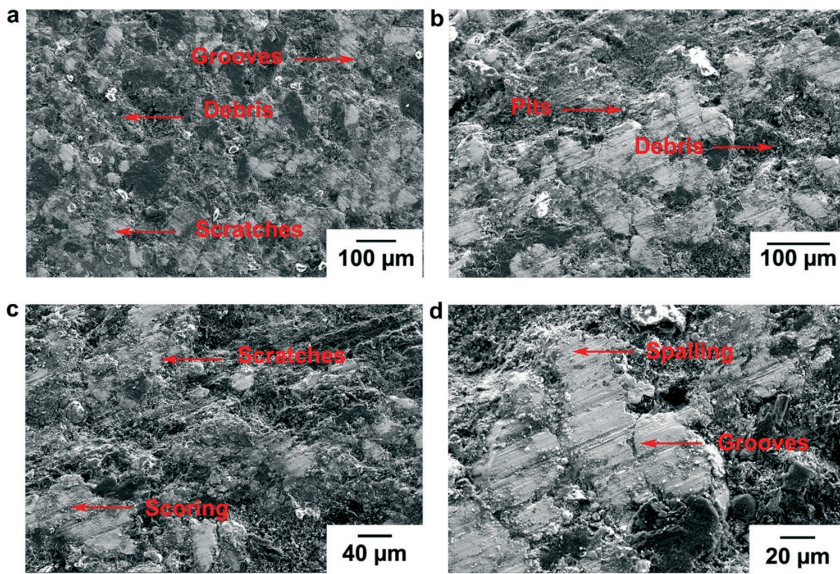
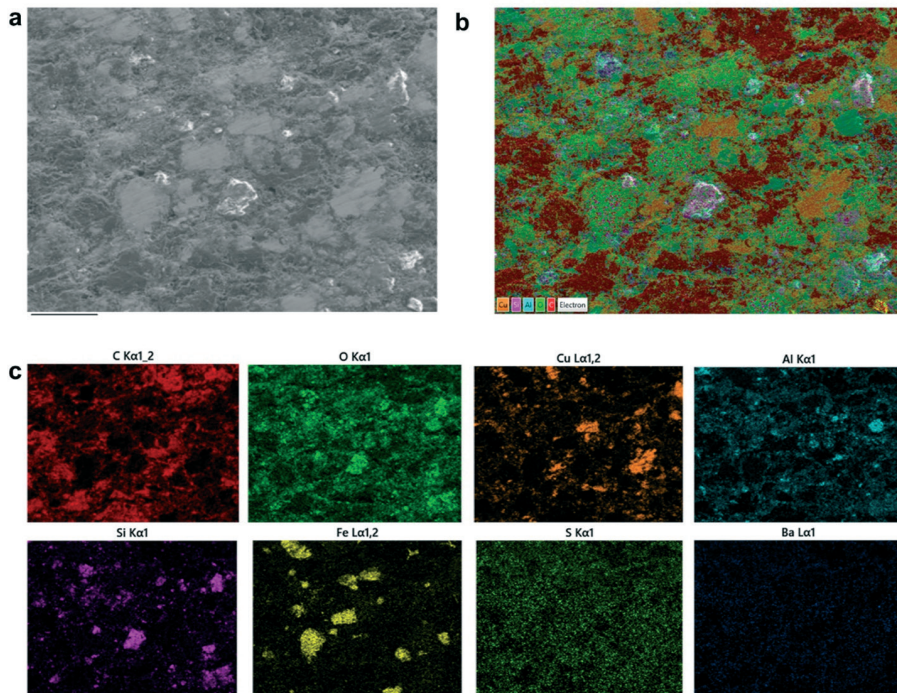Fig. 6. Surface morphology of specimen BP–20Cu–20Fe worn at a load of 30 N

Fig. 7. Elemental composition map of specimen BP–20Cu–20Fe worn at a load of 30 N

Table 2. Elemental composition worn specimens through energy dispersive x–ray spectroscopy

| Sl. | Element | Weight Concentration [%] of the Worn Specimens | | | | | |
| | | BP-20Cu-20Fe | | BP-10Cu-30Fe | | BP-0Cu-40Fe | |
		Axial Load of 30 N	Axial Load of 70 N	Axial Load of 30 N	Axial Load of 70 N	Axial Load of 30 N	Axial Load of 70 N
1	C	52.0	42.4	37.85	13.77	31.85	12.25
2	O	16.8	17.2	23.65	41.57	28.31	34.30
3	Cu	12.4	12.4	8.21	9.25	0.17	0.00
4	Fe	7.40	17.5	20.01	27.53	29.41	46.79
5	Al	4.30	3.70	3.63	2.27	3.06	2.02
6	Si	2.20	2.00	2.25	1.91	1.90	1.35
7	Ba	4.10	4.00	3.65	2.93	3.07	2.60
8	S	0.80	0.80	0.75	0.77	0.63	0.68

The composition and distribution elements are presented in Figure 7. Figure 7 (a) shows the chosen area with wear debris. Figure 7 (b) provides the consolidated elemental map that show Cu, Fe, Al, and Si maps overlap with O map. The overlap of elements indicated the formation of metal oxides (Cu/Fe) and presence of fly ash particles (Al_2O_3/SiO_2). Also, the elemental analysis given in Table 2 revealed the predominant fractions C, O, Cu, and Fe. In this condition, the worn specimen exhibits a significant presence of carbon (52.0%), indicating a predominant exposure of LDPE in the course of wear test. The moderate oxygen content (16.8%) suggested mild–oxidation during wear test. Cu (12.4%), Fe (7.4%), and minor amounts of Al (4.3%), Si (2.2%), and Ba (4.1%) contribute to the composition of the specimen [11].
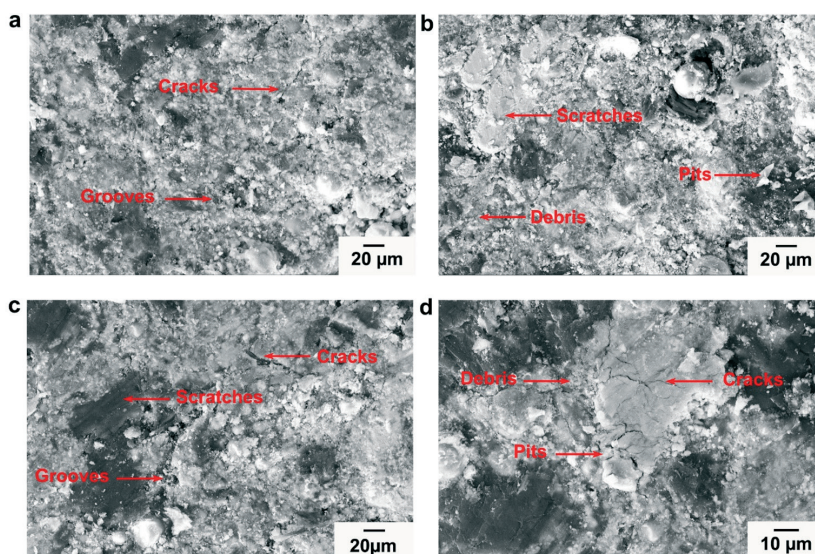

Fig. 8. Surface morphology of specimen BP-10Cu-30Fe worn at a normal load of 30 N

The worn surface morphology of the specimen BP–10Cu–30Fe is depicted in Figure 8. The specimen predominantly manifested surface irregularities in the form of scratches and pits, as shown in Figure 8 (a) and Figure 8 (b). The scratches, debris, and pits were indicative of abrasive wear and localized surface deformation. Also, the specimen exhibited the emergence of cracks, signaling the structural stresses incurred due to the heightened load conditions, as shown in Figure 8 (c) and Figure 8 (d). Additionally, fragments or chips became dislodged from the surface were observed. Table 2 shows the elemental composition of the worn specimen under 30 N axial load. The C (37.85%) was the dominant element, although slightly reduced. O content (23.65%) was comparatively higher, likely indicating oxidation during wear. Cu (8.21%) and Fe (20.01%) exhibited substantial variations in concentration, while Al (3.63%), Si (2.25%), Ba (3.65%), and S (0.75%) contribute to the composition [9].
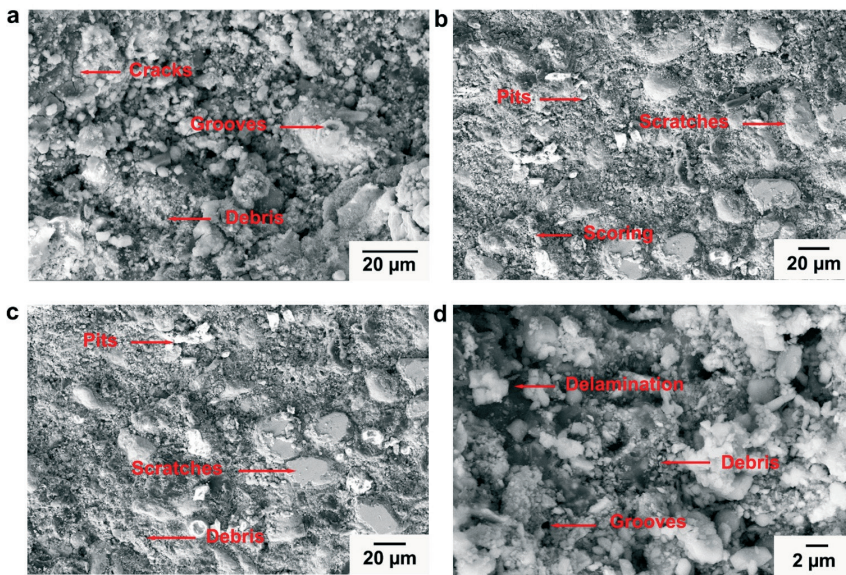

Fig. 9. Surface morphology of specimen BP–0Cu–40Fe worn at a normal load of 30 N

The surface characteristics of the cured specimen BP–0Cu–40Fe, subjected to an axial load of 30 N, are illustrated in Figure 9 Upon applying a 30 N axial load to the surface, observable material chipping, groove formation, and surface removal occur, leading to delamination. Table 2 displays elemental composition of the worn specimen BP–0Cu–40Fe under a 30 N load. C (13.77%) was present in lower quantities, while the O (38.57%) dominated the surface, suggesting severe-oxidative wear. The worn surface had Fe (39.53%), Al (2.27%), Si (1.91%), Ba (2.93%), and S (0.77%) [20].

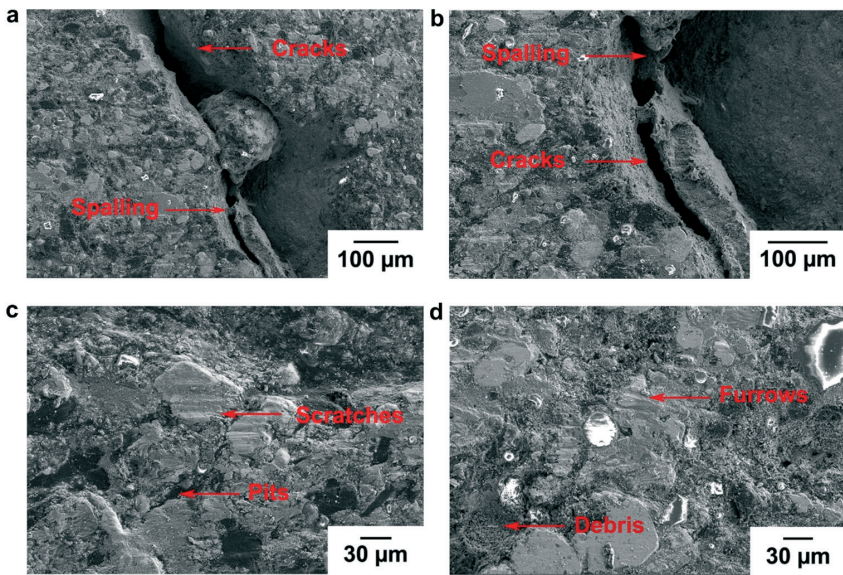**Wear Mechanism at an Axial Load of 70 N**

Fig. 10. Surface morphology of specimen BP–20Cu–20Fe worn at a normal load of 70 N
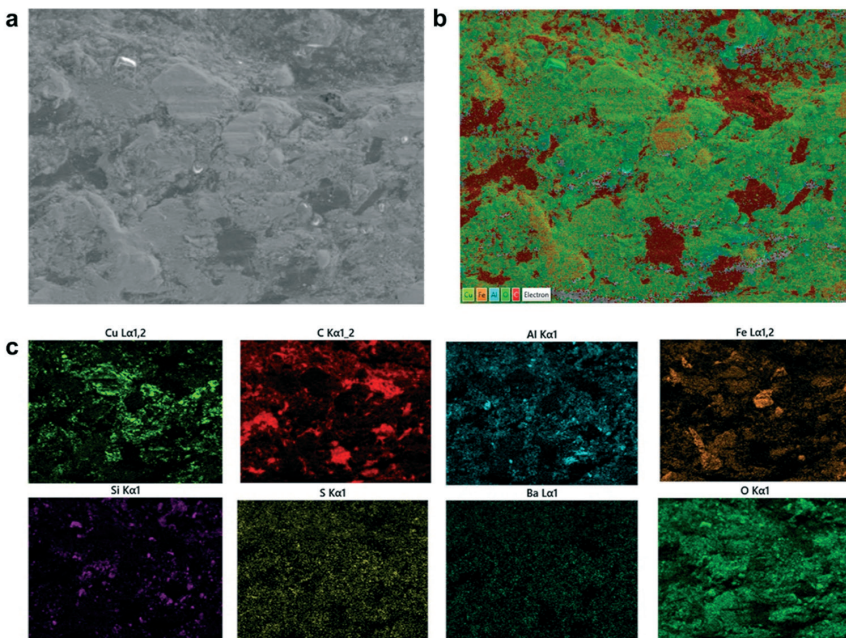

Fig. 11. Elemental composition map of specimen BP–20Cu–20Fe worn at a normal load of 70 N

The worn surface characteristics of the cured BP–20Cu–20Fe specimen, subjected to a normal load of 70 N, are presented in Figure 10. In Figure 10 (a), discernible cracks were observed on the worn surface, which were indicative of wear debris formation. The occurrence of furrows was attributed to the abrasive interaction of hard particles during the rotation of the specimen in contact with the counter disc, as shown in Figure 10 (b). The cracks become more pronounced under the influence of the 70 N load, as evident in Figure 10 (c). The material removal appeared in the form of chips, contributing to a spalling effect. Also, significant chipping and removal from the surface resulted in pits, as shown in Figure 10 (d) [28].

Figure 11 (a) provides a visual representation of the surface defects, including scratches, debris, and pits. Figure 11 (b) presents the consolidated elemental map, revealing preeminence of O on the surface the matrix. Figure 11 (c) shows the individual elemental maps confirming the homogeneous of other elements in the matrix. The overlap of elements indicates the formation of metal oxides (Cu/Fe) and the presence of fly ash particles (Al_2O_3/SiO_2). Like the specimen worn under 30 N axial load, the specimen worn at 70 N axial load continued to show C as the dominant element (42.4%). O (17.2%) remained moderate, while Cu (12.4%) and Fe (17.5%) concentrations was slightly higher. Other elements follow a similar trend as the specimen worn under 30 N axial load, with minor variations.
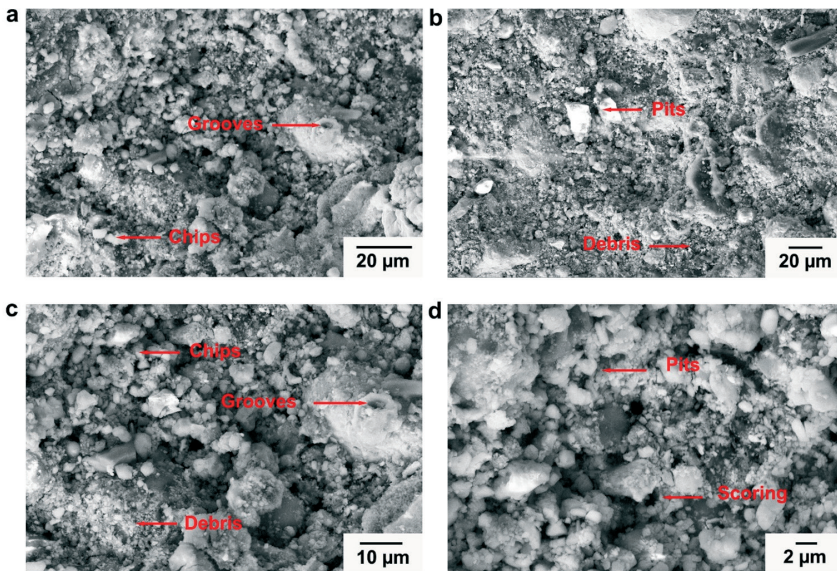

Fig. 12. Surface morphology of specimen BP–10Cu–30Fe worn at a normal load of 70 N

Figure 12 shown the surface characteristics of worn specimen BP–10Cu–30Fe when subjected to a normal load of 70 N. The specimen displayed the formation of scratches and the presence of debris without the occurrence of cracks. Figure 16 complements the analysis

by presenting the elemental composition results. The elevated oxygen content on the worn surface strongly suggests the occurrence of oxidation–induced wear. Additionally, there was an increase in the presence of Fe, which may be attributed to increased Fe concentration in the specimen. The elemental composition under the 70 N load is consistent with the 30 N load in this condition, with oxygen and iron as dominant elements, suggesting a stable wear behavior.
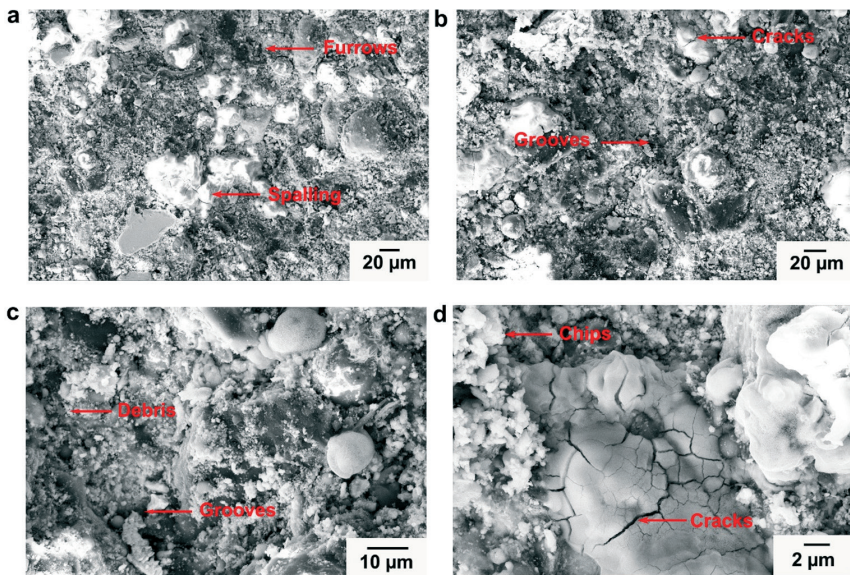

Fig. 13. Surface morphology of specimen BP–0Cu–40Fe worn at a normal load of 70 N

The surface morphology of the worn specimen BP–0Cu–40Fe is depicted in Figure 13. The specimen experienced chipping and removal from the surface, ultimately leading to delamination. Also, the specimen had material cracking, removal from the surface, and the generation of distinctive grooves. The elemental composition under the 70 N load mirrors that of the 30 N load, highlighting the consistent dominance of oxygen and iron [15].

4. Conclusion

Semi–metallic brake pads were successfully manufactured using the powder metallurgy technique, incorporating Cu, Fe, Flyash, Al_2O_3, and $BaSO_4$ as reinforcing particles. Among the fabricated specimens, specimen BP–20Cu–20Fe exhibited superior characteristics. The results demonstrated the following:

· The microstructure of the specimen BP–20Cu–20Fe displayed uniform dispersion of hard particles within the matrix. microstructure revealed a consistent dispersion of hard particles throughout the matrix, indicating a well–distributed composition.
· The specimen BP–20Cu–20Fe exhibited a microhardness of ~171 Hv.
· The specimen BP–20Cu–20Fe demonstrated superior wear resistance, with a low wear rate of 1.072×10^{-6} g/Nm observed under higher loads of 70 N. However, specimen BP–20Cu–20Fe had significant 35% rise in the friction coefficient with an increase in load from 30 N to 70 N.

5. Declarations

Author Contributions

Author	Role
P. L. Esteem	Methodology, Software, Formal analysis, Writing – Original Draft
K. Rajesh Kannan	Validation, Visualization
Dr. R. Vaira Vignesh	Conceptualization, Investigation, Writing – Review & Editing, Project administration
Dr. R. Padmanaban	Formal analysis, Resources, Supervision

Reference

Term	Definition
Conceptualization	Ideas; formulation or evolution of overarching research goals and aims
Methodology	Development or design of methodology; creation of models
Software	Programming, software development; designing computer programs; implementation of the computer code and supporting algorithms; testing of existing code components
Validation	Verification, whether as a part of the activity or separate, of the overall replication/ reproducibility of results/experiments and other research outputs
Formal analysis	Application of statistical, mathematical, computational, or other formal techniques to analyze or synthesize study data
Investigation	Conducting a research and investigation process, specifically performing the experiments, or data/evidence collection
Resources	Provision of study materials, reagents, materials, patients, laboratory samples, animals, instrumentation, computing resources, or other analysis tools
Data Curation	Management activities to annotate (produce metadata), scrub data and maintain research data (including software code, where it is necessary for interpreting the data itself) for initial use and later reuse
	Preparation, creation and/or presentation of the published work, specifically writing the initial draft (including substantive translation)
Writing – Review & Editing	Preparation, creation and/or presentation of the published work by those from the original research group, specifically critical review, commentary or revision – including pre-or postpublication stages
Visualization	Preparation, creation and/or presentation of the published work, specifically visualization/ data presentation
Supervision	Oversight and leadership responsibility for the research activity planning and execution, including mentorship external to the core team
Project administration	Management and coordination responsibility for the research activity planning and execution
Funding acquisition	Acquisition of the financial support for the project leading to this publication

6. References

[1] Akramifard H.R., Ghasemi Z.: Friction and Wear Properties of a New Semi-Metallic Brake Pad According to SAE J 661: A Case Study in PARSLENT Complex (Iran). International Journal of New Technology and Research. 2016, 2(3), 263573.

[2] Almaslow A., Ghazali M., Talib R., Ratnam C., Azhari C.: Effects of epoxidized natural rubber–alumina nanoparticles (ENRAN) composites in semi-metallic brake friction materials. Wear. 2013, 302(1–2), 1392–1396, DOI: 10.1016/j.wear.2013.01.033.

[3] Balaji M.S., Kani K.: Thermal and fade aspects of a non asbestos semi metallic disc brake pad formulation with two different resins. Advanced materials research. 2013, 622, 1559–1563, DOI: 10.4028/www.scientific.net/AMR.622-623.1559.

[4] Gudmand-Høyer L., Bach A., Nielsen G.T., Morgen P.: Tribological properties of automotive disc brakes with solid lubricants. Wear. 1999, 232(2), 168–175, DOI: 10.1016/S0043-1648(99)00142-8.

[5] Gultekin D., Uysal M., Aslan S., Alaf M., Gule, M., Akbulut H.: The effects of applied load on the coefficient of friction in Cu-MMC brake pad/Al-SiCp MMC brake disc system. Wear. 2010, 270(1–2), 73–82, DOI: 10.1016/j.wear.2010.09.001.

[6] Handa Y., Kato T.: Effects of Cu powder, $BaSO_4$ and cashew dust on the wear and friction characteristics of automotive brake pads. Tribology Transactions. 1996, 39(2), 346–353, DOI: 10.1080/10402009608983537.

[7] Hu B.: Roles of iron metal powders in semi-metallic friction materials. Seventh International Technical Exchange and Products Exhibition on Friction Materials. Wuhan, China, June 16–18 2005.

[8] Hussain S., Abdul Hamid M., Mat Lazim A., Abu Bakar A.: Brake wear particle size and shape analysis of non-asbestos organic (NAO) and semi metallic brake pad. Jurnal Teknologi, 2014, 71(2), DOI: 10.11113/jt.v71.3731.

[9] Jaafar T.R., Selamat M.S., Kasiran R.: Selection of best formulation for semi-metallic brake friction materials development. Powder metallurgy. 2012, 1–30, DOI: 10.5772/33909.

[10] Kachhap R.K., Satapathy B.K.: Synergistic effect of tungsten disulfide and cenosphere combination on braking performance of composite friction materials. Materials & Design (1980–2015). 2014, 56, 368–378, DOI: 10.1016/j.matdes.2013.11.006.

[11] Kchaou M., Sellami A., Elleuch R., Singh H.: Friction characteristics of a brake friction material under different braking conditions. Materials & Design (1980–2015). 2013, 52, 533–540, DOI: 10.1016/j.matdes.2013.05.015.

[12] Keshav M.G., Hemchandran C., Dharsan B., Pradhin K., Vignesh R.V., Govindaraju M.: Manufacturing of continuous fiber reinforced sintered brake pad and friction material. Materials Today: Proceedings. 2021, 46, 4493–4496, DOI: 10.1016/j.matpr.2020.09.686.

[13] Kukutschová J., Roubíček V., Mašláň M., Jančík D., Slovák V., Malachová, K., et al.: Wear performance and wear debris of semimetallic automotive brake materials. Wear. 2010, 268(1–2), 86–93, DOI: 10.1016/j.wear.2009.06.039.

[14] Kumar M., Bijwe J.: NAO friction materials with various metal powders: Tribological evaluation on full-scale inertia dynamometer. Wear. 2010, 269(11–12), 826–837, DOI: 10.1016/j.wear.2010.08.011.

[15] Kumar S., Ghosh S.K.: Porosity and tribological performance analysis on new developed metal matrix composite for brake pad materials. Journal of Manufacturing Processes. 2020, 59, 186–204, DOI: 10.1016/j.jmapro.2020.09.053.

[16] Matějka V., Lu Y., Fan Y., Kratošová G., Lešková J.: Effects of silicon carbide in semi-metallic brake materials on friction performance and friction layer formation. Wear,2008, 265(7–8), 1121–1128, DOI: 10.1016/j.wear.2008.03.006.

[17] Matějka V., Perricone G., Vlček J., Olofsson U., Wahlström J.: Airborne wear particle emissions produced during the dyno bench tests with a slag containing semi-metallic brake pads. Atmosphere. 2020, 11(11), 1220, DOI: 10.3390/atmos11111220.

[18] Mohanty S., Chugh Y.: Development of fly ash–based automotive brake lining. Tribology International. 2007, 40(7), 1217–1224, DOI: 10.1016/j.triboint.2007.01.005.

[19] Österle W., Griepentrog M., Gross T., Urban I.: Chemical and microstructural changes induced by friction and wear of brakes. Wear. 2001, 250–251(Part 2), 1469–1476, DOI: 10.1016/S0043-1648(01)00785-2.

[20] Österle W., Urban I.: Friction layers and friction films on PMC brake pads. Wear. 2004, 257(1–2), 215–226, DOI: 10.1016/j.wear.2003.12.017.

[21] Parikh H.H., Gohil P.P.: Tribology of fiber reinforced polymer matrix composites—A review. Journal of Reinforced Plastics and Composites. 2015, 34(16), 1340–1346, DOI: 10.1177/0731684415591199.

[22] Pinca-Bretotean C., Josan A., Birtok-Băneasă C.: Laboratory testing of brake pads made of organic materials intended for small and medium vehicles. IOP conference series: materials science and engineering. 2018, DOI: 10.1088/1757-899X/393/1/012029.

[23] Rajan R., Tyagi Y., Das A., Kumar P., Patel S.K.: Development and analysis of friction characteristics of coir fiber added organic brake pad composite. Materials Today: Proceedings. 2022, 62, 6077–6082, DOI: 10.1016/j.matpr.2022.04.1011.

[24] Rhee S.: Brake wear. MFPG, Product Durability and Life. Proceedings of the 27th Meeting of the Mechanical Failures Prevention Group, Held at the National Bureau of Standards, Gaithersburg, Maryland, 1977, 1–3.

[25] Tang C.-F., Lu Y.: Combinatorial screening of ingredients for steel wool based semimetallic and aramid pulp based nonasbestos organic brake materials. Journal of reinforced plastics and composites. 2004, 23(1), 51–63, DOI: 10.1177/0731684044028701.

[26] Tokala V.N.B., Kanneganti C.A., Kesana N.: Comparative Study on Dynamometer Performance Evaluation of Fly Ash Containing Organic and Semi-Metallic Motorcycle Disc Brake Pads. International Journal of Mechanical and Production Engineering Research and Development. 2018, 8(3), 227–234, DOI: 10.24247/ijmperdjun201826.

[27] Xiao Y., Cheng Y., Shen M., Yao P., Du J., Ji D., et al.: Friction and wear behavior of copper metal matrix composites at temperatures up to 800 C. Journal of Materials Research and Technology. 2022, 19, 2050–2062, DOI: 10.1016/j.jmrt.2022.05.192.

[28] Xiao Y., Zhang Z., Yao P., Fan K., Zhou H., Gong T., et al.: Mechanical and tribological behaviors of copper metal matrix composites for brake pads used in high-speed trains. Tribology International. 2018, 119, 585–592, DOI: 10.1016/j.triboint.2017.11.038.

[29] Yu J., He J., Ya C.: Preparation of phenolic resin/organized expanded vermiculite nanocomposite and its application in brake pad. Journal of Applied Polymer Science. 2011, 119(1), 275–281, DOI: 10.1002/app.32557.